

## Direct Observation of Infrared Plasmonic Fano Antiresonances by a Nanoscale Electron Probe

Kevin C. Smith<sup>1</sup>, Agust Olafsson<sup>1</sup>, Xuan Hu<sup>2</sup>, Steven C. Quillin<sup>3</sup>, Juan Carlos Idrobo<sup>4</sup>, Robyn Collette,<sup>5</sup> Philip D. Rack<sup>5,4</sup>, Jon P. Camden<sup>1,2,5,\*</sup>, and David J. Masiello<sup>3,†</sup>

<sup>1</sup>*Department of Physics, University of Washington, Seattle, Washington 98195, USA*

<sup>2</sup>*Department of Chemistry and Biochemistry, University of Notre Dame, Notre Dame, Indiana 46556, USA*

<sup>3</sup>*Department of Chemistry, University of Washington, Seattle, Washington 98195, USA*

<sup>4</sup>*Center for Nanophase Materials Sciences, Oak Ridge National Laboratory, Oak Ridge, Tennessee 37831, USA*

<sup>5</sup>*Department of Materials Science and Engineering, University of Tennessee, Knoxville, Tennessee 37996, USA*



(Received 2 August 2019; published 21 October 2019)

In this Letter, we exploit recent breakthroughs in monochromated aberration-corrected scanning transmission electron microscopy (STEM) to resolve infrared plasmonic Fano antiresonances in individual nanofabricated disk-rod dimers. Using a combination of electron energy-loss spectroscopy and theoretical modeling, we investigate and characterize a subspace of the weak coupling regime between quasidiscrete and quasicontinuum localized surface plasmon resonances where infrared plasmonic Fano antiresonances appear. This work illustrates the capability of STEM instrumentation to experimentally observe nanoscale plasmonic responses that were previously the domain only of higher-resolution infrared spectroscopies.

DOI: 10.1103/PhysRevLett.123.177401

Since the pioneering work of Ruthemann in 1941 [1], inelastic electron scattering experiments using collimated electron beams have made enormous advances in their ability to simultaneously combine and correlate spectroscopic information with spatial imaging at the nanoscale. Today, electron energy-loss spectroscopy (EELS) performed in a monochromated aberration-corrected scanning transmission electron microscope (STEM) can resolve energy losses below 5 meV, with a focused fast electron probe that possesses qualities similar to an ultrafast, near-field, white light source and is only a few atoms in diameter [2]. Paired with modern developments in instrumentation, these properties of the electron probe have made possible the simultaneous spectroscopy and nanometer-scale imaging of optically bright and dark electronic, and even vibrational, excitations in nanoparticles [3–13], plasmonic energy and charge transfer [14–16], and magneto-optical metamaterials [17–21], heralding a new frontier of materials discovery that is inaccessible to far-field optical spectroscopies.

Despite these advances, the asymmetric Fano line shape [22], first observed in 1959 in the EEL autoionization spectrum of He gas [23,24], remains elusive in the EELS of plasmonic systems. In his seminal 1961 work [22], Fano interpreted the observed line shapes in terms of a configuration interaction between helium's discrete  $2s2p$  double electronic excitation and the scattering continuum. In recent years, so-called Fano interferences or antiresonances have been observed in a variety of optical [25–31], plasmonic [32–39], and transport [40–42] experiments that involve weak coupling between spectrally narrow and broad resonances as generalizations of Fano's original discrete

and continuum states. Theory has debated the ability of EELS to capture the Fano antiresonance in plasmonic systems [43–45], providing impetus for a careful experimental investigation.

Motivated by a new generation of STEM monochromators, we construct and measure the spectral response of a plasmonic nanostructure that satisfies two critical requirements for the Fano antiresonance: (i) the individual plasmonic “configurations” are weakly coupled to each other, and (ii) there is roughly a factor of 10 or greater between the linewidths of each configuration, corresponding to the discrete and continuum channels of Fano's original analysis. These requirements are achieved through the design of a gold disk-rod dimer possessing a series of sharp, experimentally resolvable midinfrared Fano antiresonances arising from the perturbative influence of the rod's spectrally narrow infrared Fabry-Pérot (FP) surface plasmon polariton (SPP) resonances [46–51] upon the comparably broad dipole plasmon of the disk. We also present an analytical model that generalizes the Fano line shape to account for the finite linewidth of both broad (quasicontinuum) and narrow (quasidiscrete) modes, as well as the inherently lossy nature of the interaction between rod and disk modes through the electromagnetic field. Finally, we apply the model to the experimentally measured dimer spectra, showing that it explains the observed features in terms of the incoherent interaction between the rod and disk plasmons in rationally designed dimers of variable disk diameter and rod length.

Figure 1(a) shows a schematic of the coupled disk-rod system studied, designed such that the disk dipole plasmon

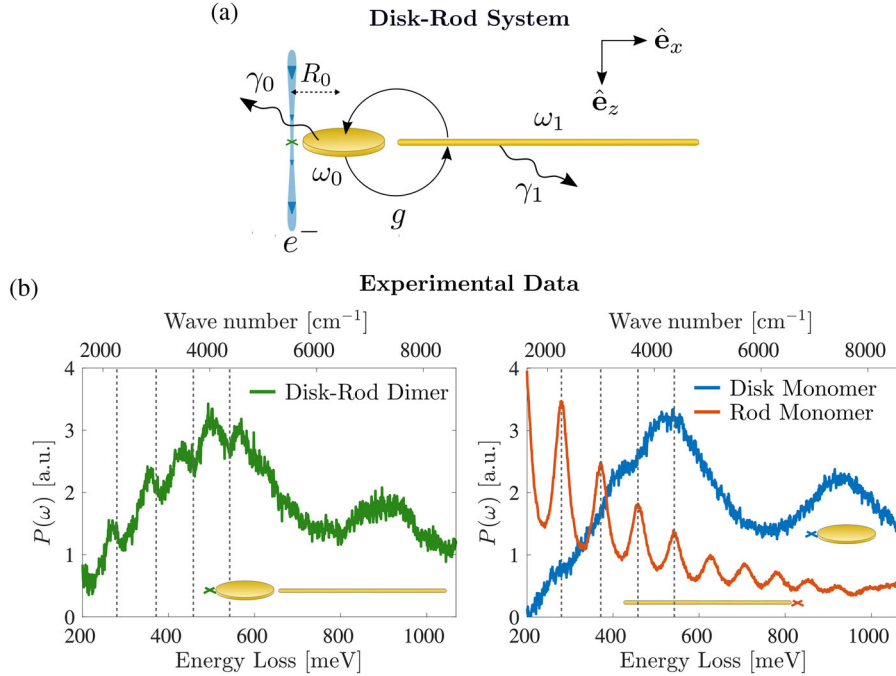


FIG. 1. (a) Schematic of a gold disk-rod dimer indicating the relevant system parameters and electron-beam location where spectra are acquired (green  $\times$ ). (b) Experimental EEL spectrum of a dimer consisting of an 800-nm-diameter gold disk and a 5- $\mu\text{m}$ -long gold rod separated by a 50 nm gap (green curve). Blue and red curves show the monomer spectra for a near-identical disk and rod, respectively. The dimer spectrum is not a simple sum of the two monomer spectra but instead exhibits a narrow dip at the spectral location of each rod mode. A typical example of the EEL spectrum acquired at the rod end may be found in Supplemental Material [52].

resonance spans a progression of narrow FP rod modes of alternating parity. Tuning the rod length controls the number of rod modes that overlap with the disk dipole, while both the rod length and disk diameter together determine the degree of spectral overlap between disk and rod modes. Weak coupling is achieved at relatively large disk-rod separations ( $\sim 50$  nm edge to edge), with the parameters necessary for Fano antiresonances falling into a subset of this space where, in addition, there is a factor of  $\sim 10$  or greater between the disk dipole plasmon and FP rod resonance linewidths. Extensive preliminary experimental and theoretical studies were performed to optimize the plasmon energies and linewidths of the disk and rod monomers such that the disk-rod dimers meet these criteria while retaining the smallest detuning possible between the disk dipole and lower-order rod modes.

The left panel in Fig. 1(b) shows the point EEL spectrum of a disk-rod dimer measured at a beam location 10 nm radially outward from the disk edge (green  $\times$ ). For comparison, the right panel in Fig. 1(b) displays the

EEL spectra for an isolated disk (blue curve) and rod (red curve) of the same size as in the dimer, collected at beam locations indicated by the blue and red  $\times$ . The disk monomer spectrum reveals a broad resonance around 500 meV attributed to the dipolar disk mode, while the rod monomer spectrum shows a succession of spectrally narrow FP SPP resonances beginning around 200 meV. As anticipated, the spectrum of the coupled system collected on the disk end is not a simple sum of the two monomer spectra but instead follows the Lorentzian-like ‘envelope’ of the isolated disk dipole peak with narrow asymmetric dips at the spectral location of each rod mode (dotted lines), indicative of weak coupling.

Analysis and interpretation of measured EEL spectra is facilitated by analytical modeling of the disk-rod dimer. Considering only the interaction between a single FP mode of the rod with the dipole plasmon of the disk, the surface plasmon resonance solutions of Maxwell’s equations can be mapped onto the following set of coupled harmonic oscillators [10,19]:

$$\begin{aligned} \ddot{p}_0 + \gamma_{\text{nr}} \dot{p}_0 - \frac{2e^2}{3m_0 c^3} \ddot{p}_0 + \omega_0^2 p_0 - \sqrt{\frac{m_1}{m_0}} \int_{-\infty}^t dt' g(t-t') p_1(t') &= \frac{e^2}{m_0} E_{\text{el}}^x(\mathbf{0}, t), \\ \ddot{p}_1 + \gamma_{\text{nr}} \dot{p}_1 + \gamma_{\text{rad}} \dot{p}_1 + \omega_1^2 p_1 - \sqrt{\frac{m_0}{m_1}} \int_{-\infty}^t dt' g(t-t') p_0(t') &= 0. \end{aligned} \quad (1)$$

Here  $p_i$  labels the  $x$ -oriented surface plasmons of the disk ( $i = 0$ ) and rod ( $i = 1$ ) of natural frequency  $\omega_i$ , non-radiative dissipation rate  $\gamma_{\text{nr}}$ , and effective mass  $m_i$  [10,19]. Radiation-reaction forces have been included to account for radiative losses by the system, which in the frequency domain can be repackaged into the total dissipation rates  $\gamma_0(\omega) = \gamma_{\text{nr}} + 2e^2\omega^2/3m_0c^3$  for the disk dipole mode [53] and  $\gamma_1 = \gamma_{\text{nr}} + \gamma_{\text{rad}}$  for the rod mode; here  $\gamma_{\text{rad}}$  has been used in place of the frequency-dependent Larmor rate due to the nondipolar nature of the rod modes, which are sufficiently spectrally narrow such that  $\gamma_{\text{rad}}$  is well approximated as frequency independent.

The disk dipole plasmon is driven by the electric field  $\mathbf{E}_{\text{el}}(\mathbf{x}, t) = -e(\mathbf{x} - \mathbf{R}_0 - \mathbf{v}t)/\gamma_L^2[(z - vt)^2 + (R/\gamma_L)^2]^{3/2}$  of the fast electron moving uniformly with velocity  $\mathbf{v} = \hat{\mathbf{e}}_z v$  evaluated at the center of the disk, taken to be the origin. Here  $\gamma_L = [1 - (v/c)^2]^{-1/2}$  is the Lorentz contraction factor,  $\mathbf{R}_0 = -\hat{\mathbf{e}}_x R_0$  is the electron beam position [Fig. 1(a), green  $\times$ ], and  $R = \sqrt{(x + R_0)^2 + y^2}$  is the lateral distance between the electron probe and field observation point in the impact plane ( $z = 0$ ). Because of the relatively large disks studied ( $\gtrsim 650$  nm in diameter), the rod modes are not directly driven by the evanescent field of the electron when the electron probe is positioned at the disk end of the dimer. No EEL signal is observable above the background when the disk is removed, illustrating the disk's role as an antenna that transfers energy from the electron probe to the rod.

The coupling strength between the disk and rod plasmon modes depends upon the relative separation and orientation of the disk and rod as well as their respective polarizabilities. In the frequency domain, the coupling is characterized by the complex parameter  $g(\omega)$ , arising from the interaction energy  $U_{\text{int}} = -\mathbf{E}_1 \cdot \mathbf{p}_0$ , where  $\mathbf{E}_1$  is the induced electric field of the rod mode evaluated at the disk dipole center. The real part of  $g(\omega)$  defines the rate of energy transfer between the disk and rod plasmon modes, while the imaginary part accounts for the lossy nature of this interaction and is related to the degree of interference between the fields of the coupled modes [52]. Because the rod modes are spectrally narrow, the real part of the coupling strength  $g(\omega)$  may be treated as approximately frequency independent. Likewise, the imaginary part is taken to be linear in  $\omega$ , as  $g(\omega)$  is purely real for static fields (i.e.,  $\omega = 0$ ) and, therefore, does not have a frequency-independent contribution. Lastly, only the coupled plasmon dynamics oriented parallel to the rod's long axis need be considered due to the high aspect ratio of the rod, justifying the use of the quasi-one-dimensional dynamical equations in Eq. (1) with all other collective electronic motion occurring at much higher energies.

The EEL probability  $P(\omega)$  per unit frequency  $\omega$  of transferred quanta between the electron beam and target is obtained by computing the work done on the electron probe by the field induced in the polarized target [54]:

$$P(\omega) = \frac{|\tilde{E}_{\text{el}}^x(\mathbf{0}, \omega)|^2}{\pi\hbar} \times \text{Im} \left[ \frac{e^2}{m_0} \left( \omega_0^2 - \omega^2 - i\omega\gamma_0 - \frac{g^2}{\omega_1^2 - \omega^2 - i\omega\gamma_1} \right)^{-1} \right], \quad (2)$$

while the EEL probability for the isolated disk  $P_0(\omega)$  is obtained from the above expression by taking  $g = 0$ . The ratio between  $P(\omega)$  and  $P_0(\omega)$  at the same beam position  $\mathbf{R}_0$  can be cast into the reduced form

$$\frac{P(\omega)}{P_0(\omega)} = \left[ 1 + \text{Im} \left( \frac{g^2/\omega\gamma_0}{\omega_1^2 - \omega^2 - i\omega\gamma_1} \right) \right] \left| \frac{q + \epsilon}{\epsilon + i} \right|^2, \quad (3)$$

which generalizes Fano's original line shape to account for dissipation in both broad and narrow plasmon resonances as well as complex coupling. Here  $q(\omega) = [\Omega^2(\omega) - \omega_1^2 + i\omega\gamma_1(\omega)]/\omega\Gamma(\omega)$  and  $\epsilon(\omega) = [\omega^2 - \Omega^2(\omega)]/\omega\Gamma(\omega)$  are, respectively, the complex-valued asymmetry function and reduced frequency expressed in terms of the modified frequency  $\Omega^2(\omega) = \omega_1^2 - \text{Re}[g^2(\omega_0^2 - \omega^2 - i\omega\gamma_0)^{-1}]$  and linewidth  $\Gamma(\omega) = \gamma_1(\omega) + (1/\omega)\text{Im}[g^2(\omega_0^2 - \omega^2 - i\omega\gamma_0)^{-1}]$  of the spectral feature described by the interaction of the disk dipole and rod plasmon modes. For true Fano antiresonances, the function  $q(\omega) \approx q(\omega_1)$  is approximately constant and represents the asymmetry parameter originally proposed by Fano to distill the physics of the antiresonance into a single number that depends upon the basic system parameters [22]. Here, since both disk and rod modes are dissipative, the asymmetry parameter generalizes to a complex-valued number, the real part of which characterizes the degree of asymmetry of the antiresonance. It is important to note that, without the second term proportional to  $\gamma_1$ ,  $q(\omega)$  would be real valued and the reduced EEL probability spectrum [Eq. (3)] would vanish whenever  $\epsilon(\omega) = -q(\omega)$  [27]. However, this is not observed experimentally at any coupling strength due to the finite linewidth of the spectrally narrow rod resonances. Lastly, the standard form of the Fano line shape is scaled by a frequency-dependent prefactor which accounts for the additional nondisk dissipation channels of the dimer.

Since each rod has multiple plasmon modes that spectrally overlap the disk dipole plasmon resonance, the EEL probability is further generalized as

$$P(\omega) = \frac{|\tilde{E}_{\text{el}}^x(\mathbf{0}, \omega)|^2}{\pi\hbar} \times \text{Im} \left[ \left( \omega_0^2 - \omega^2 - i\omega\gamma_0 - \sum_j \frac{g_j^2}{\omega_j^2 - \omega^2 - i\omega\gamma_j} \right)^{-1} \right], \quad (4)$$

and the reduced EEL probability may be cast into the approximate form

$$\frac{P(\omega)}{P_0(\omega)} \approx \prod_{j=1}^N \mathcal{F}_j(q_j(\omega), \epsilon_j(\omega)), \quad (5)$$

where  $\mathcal{F}_j(q_j(\omega), \epsilon_j(\omega))$  is the Fano line shape describing the interaction between the  $j$ th rod plasmon mode and the disk dipole plasmon mode (labeled by the subscript 0) given by Eq. (3). This product factorization of the reduced spectrum, which allows for an estimate of the asymmetry function  $q_j(\omega)$  for each individual rod plasmon mode, is approximate as the rod resonances overlap weakly, causing their individual contribution to the dimer spectrum to depend upon neighboring rod modes through their mutual interaction with the disk dipole plasmon. Nonetheless, the exact form of the reduced EEL spectrum inferred from Eq. (4) can be used to demonstrate the accuracy of the simple product form in the weak coupling regime when all rod modes are well separated spectrally [52]. Lastly, while the model parameters (including  $g_j$ ) could be obtained by approximating the disk and rod by oblate and prolate spheroids and adding the contributions from radiation damping, doing so adds little additional insight into the measurements; thus, we obtain these parameters by numerically fitting the experimental spectra.

Measured EEL spectra are collected at  $\mathbf{R}_0$  for a set of fabricated gold disk-rod dimers of varying rod lengths and disk diameters. All system parameters ( $\omega_0, m_0, \omega_j, \gamma_j$ , and  $g_j$ ) are obtained for each dimer by least-squares fitting the

analytic form for  $P(\omega)$  defined by Eq. (4) to the spectra. The nonradiative (Drude) dissipation rate of the disk dipole is set prior to fitting according to the value for gold at optical frequencies ( $\hbar\gamma_{\text{Au}} = 69$  meV [55]). Initial guesses for the natural frequency  $\omega_0$  and effective mass  $m_0$  of the disk plasmon are estimated for each dimer by fitting the measured EEL spectra collected at  $\mathbf{R}_0$  of an isolated disk, while initial guesses for  $\omega_j$  and  $\gamma_j$  of the  $N$  rod plasmons are estimated from the EEL spectra of an isolated rod. To check the fitting procedure, the parameters obtained from each dimer spectrum are used to reconstruct the disk monomer spectrum  $P_0(\omega)$ , rod monomer spectrum  $P_{\text{rod}}(\omega) = \sum_j P_j(\omega)$  [where  $P_j(\omega)$  is identical in form to  $P_0(\omega)$  with indices interchanged where appropriate], and the reduced EEL probability spectrum  $P(\omega)/P_0(\omega)$  for each structure. We note that, while any spectrum can be fit by an arbitrary collection of oscillators, the approach here is restricted by the number of oscillators present in the monomer spectra.

Figure 2 shows the result of this analysis for another dimer. The point EEL spectrum, collected at an equivalent beam position to that in Fig. 1(b), is shown in the upper panel in Fig. 2(a) (green bullets) with the fit to Eq. (4) overlaid (black curve). The bottom panel in Fig. 2(a) compares the experimental EEL spectra obtained from a 650 nm disk monomer (blue bullets) and a 5  $\mu\text{m}$  rod monomer (red bullets) to the theoretical monomer spectra reconstructed from parameters obtained from fitting the

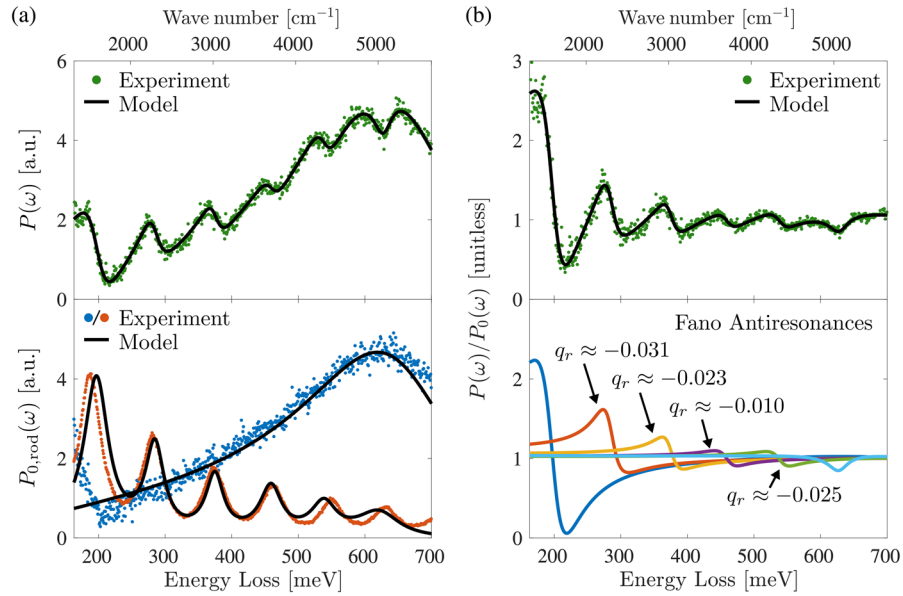


FIG. 2. EEL point spectrum of a gold disk-rod dimer composed of a 650-nm-diameter disk and a 5  $\mu\text{m}$  rod separated by a 50 nm gap. The spectrum exhibits a progression of infrared Fano antiresonances due to the interaction between the broad disk dipole plasmon resonance and the spectrally narrow plasmon modes of the rod. The upper panels display the (a) experimental (green curve) and fit (black curve) EEL spectrum and (b) reduced EEL spectrum of the dimer collected at the disk end. The lower panel in (a) shows the experimental monomer spectra of an isolated disk (blue curve) and rod (red curve). As an independent check of the fitting procedure, the theoretical monomer spectra are reconstructed from the dimer fit parameters (black curves), showing excellent agreement. The lower panel in (b) displays the decomposition of each antiresonance in the reduced spectrum into a product of Fano line shapes  $\mathcal{F}_j(q_j, \epsilon_j)$  as described in Eq. (5) with the corresponding value of the real part of the asymmetry parameter  $q_{r,j} = \text{Re } q_j(\omega_j)$  indicated above each feature.

dimer spectrum (black curve). Because of small geometrical variations between the isolated monomer rods and disks versus those which compose the dimers, the monomer spectra will not, in general, exactly match those corresponding to the dimer disk and rod. In addition, deviation between the reconstructed and experimental disk monomer spectra is expected on the higher-energy side of the disk dipole peak, where the quadrupole plays a non-negligible dynamical role. Despite these limitations, Fig. 2(a) shows excellent agreement between reconstructed and experimental spectra, which further validates our ability to extract the monomer parameters from the dimer spectra. To compare with our theoretical analysis, Fig. 2(b) displays the reduced EEL probability (green bullets) obtained by dividing the experimental spectrum by the theoretically reconstructed isolated disk spectrum  $P_0(\omega)$  (top), along with the decomposition into a progression of individual Fano line shapes  $\mathcal{F}_j(q_j, \epsilon_j)$  (bottom).

This analysis is repeated for a set of four unique disk-rod combinations [52] and summarized in Fig. 3 to illustrate the variation in coupling strength and relative linewidth as a function of the disk and rod size. Underlying each data point is a particular rod FP mode (labeled  $j$ ) which interacts with the disk dipole plasmon (labeled 0). All point EEL spectra are collected 10 nm radially outward along the rod long axis from the disk edge [Fig. 1(b), green  $\times$ ]. As each

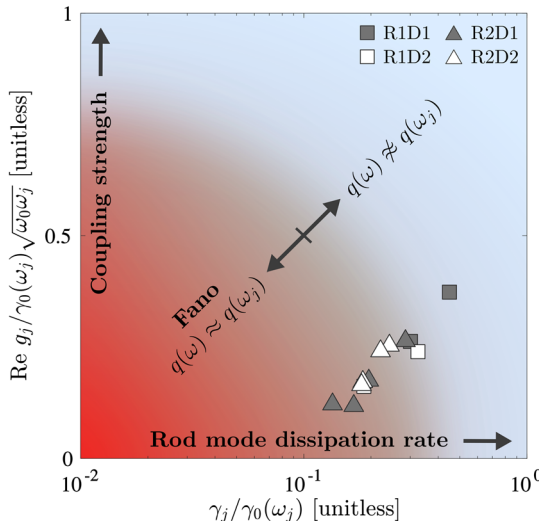


FIG. 3. Graphical summary of the interaction between individual rod resonances and the disk dipole plasmon in a collection of disk-rod dimers. Each mode pair is represented by a distinct symbol and is characterized by its relative coupling strength  $\text{Re } g_j/\gamma_0(\omega_j)\sqrt{\omega_0\omega_j}$  and dissipation rate  $\gamma_j/\gamma_0(\omega_j)$ . Dimers denoted by  $R1$  ( $R2$ ) consist of 2.5- $\mu\text{m}$ - (5- $\mu\text{m}$ -) long rods, while those denoted by  $D1$  ( $D2$ ) consist of 650-nm- (800-nm-) diameter disks. In all dimers, the disk and rod are separated by a gap of 50 nm, and, since  $\text{Re } g_j/\gamma_0(\omega_j)\sqrt{\omega_0\omega_j} = 1$  denotes the boundary between weak and strong coupling, all dimers are in the weak coupling regime. The gray triangle symbols indicate specific Fano antiresonances shown explicitly in Fig. 2.

dimer contains multiple overlapping disk and rod modes, these four structures generate 12 modes available for analysis. For all dimers, the lowest- and highest-energy rod resonances are not included as explicit data points due to uncertainties imposed by subtraction of the zero-loss peak and interactions with the  $\text{SiO}_2$  substrate phonon mode at lower energies ( $\lesssim 200$  meV) and the influence of the disk quadrupole at higher energies ( $\gtrsim 650$  meV). The full spectra, however, are displayed in Supplemental Material [52].

All disk-rod mode pairs are found to be in the weak coupling regime, as each data point satisfies the inequality  $\text{Re } g_j/\gamma_0(\omega_j)\sqrt{\omega_0\omega_j} < 1$  [56,57]. Additionally, multiple disk-rod mode pairs are found to obey the linewidth condition  $\gamma_j \sim \gamma_0/10$  (Fig. 3, red region), including those highlighted in Fig. 2, thus satisfying both requirements for the emergence of Fano antiresonances in the coupled spectrum. Additionally, these results indicate that the size of both the rod and the disk plays a crucial role in determining whether the disparity in linewidths between the disk and rod modes is sufficient to observe a sharp antiresonance. We find that the longer 5  $\mu\text{m}$  rods ( $R2$ ) in combination with the 650-nm-diameter disk ( $D1$ ) optimally balance the two criteria for sharp Fano antiresonances while supporting a progression of rod modes which are minimally detuned from the disk dipole such that disk-rod interaction is non-negligible.

In conclusion, we resolve for the first time Fano antiresonances in the EEL spectrum of a plasmonic nanostructure. This is achieved by rationally designing a gold disk-rod dimer supporting rod resonances that are spectrally narrow relative to the disk dipole. The observation of the asymmetric line shapes is facilitated by a new generation of monochromated and aberration-corrected STEMs which open the infrared spectral region to interrogation. We develop a theoretical model which generalizes the original Fano line shape to account for dissipation in both the quasidiscrete and the quasicontinuum channels in STEM EELS. This analysis makes explicit the classification of the observed dimer line shapes in terms of the asymmetry parameter  $q$ , as discovered in the autoionization spectrum of He by Fano in 1961 [22]. This combined experimental and theoretical work not only resolves an ongoing discussion in the literature about the existence of Fano line shapes in the EELS of plasmonic systems [43–45], but also showcases the ability of the latest generation of monochromated STEMs to observe spectrally narrow plasmonic responses that were previously the domain only of higher-resolution optical spectroscopies.

We thank Yueying Wu, Xiang-Tian Kong, Zhongwei Hu, and Jacob A. Busche for preliminary experimental and numerical efforts which led to the work presented. This work was supported by the University of Washington, the University of Notre Dame, the University of Tennessee, the

U.S. Department of Energy Basic Energy Sciences under Grants No. DE-SC0018040 for the theoretical modeling and numerical simulation of the electron probe (K. C. S., S. C. Q., and D. J. M.), No. DE-SC0018169 for the EELS measurements and analysis (A. O., X. H., and J. P. C.), and National Science Foundation No. DMR-1709275 (R. C. and P. D. R.) for the nanofabrication of the dimer heterostructures. The STEM experiments and dimer nanofabrication were conducted at the Center for Nanophase Materials Sciences, which is a DOE Office of Science User Facility (J. C. I., P. D. R.). This research was conducted, in part, using instrumentation within ORNL's Materials Characterization Core provided by UT-Batelle, LLC under Contract No. DE-AC05-00OR22725 with the U.S. Department of Energy and sponsored by the Laboratory Directed Research and Development Program of Oak Ridge National Laboratory, managed by UT-Battelle, LLC, for the U.S. Department of Energy.

<sup>\*</sup>jon.camden@nd.edu

<sup>†</sup>masiello@uw.edu

[1] G. Ruthemann, *Naturwissenschaften* **29**, 648 (1941).

[2] O. L. Krivanek, T. C. Lovejoy, N. Dellby, and R. Carpenter, *Microscopy* **62**, 3 (2013).

[3] F. J. García de Abajo, *Rev. Mod. Phys.* **82**, 209 (2010).

[4] N. W. Bigelow, A. Vaschillo, V. Iberi, J. P. Camden, and D. J. Masiello, *ACS Nano* **6**, 7497 (2012).

[5] O. L. Krivanek, T. C. Lovejoy, N. Dellby, T. Aoki, R. W. Carpenter, P. Rez, E. Soignard, J. Zhu, P. E. Batson, M. J. Lagos, R. F. Egerton, and P. A. Crozier, *Nature (London)* **514**, 209 (2014).

[6] M. J. Lagos, A. Trügler, U. Hohenester, and P. E. Batson, *Nature (London)* **543**, 529 (2017).

[7] H. Lourenço-Martins and M. Kociak, *Phys. Rev. X* **7**, 041059 (2017).

[8] M. Kociak and O. Stéphan, *Chem. Soc. Rev.* **43**, 3865 (2014).

[9] Y. Wu, G. Li, and J. P. Camden, *Chem. Rev.* **118**, 2994 (2018).

[10] C. Cherqui, N. Thakkar, G. Li, J. P. Camden, and D. J. Masiello, *Annu. Rev. Phys. Chem.* **67**, 331 (2016).

[11] A. L. Koh, A. I. Fernández-Domínguez, D. W. McComb, S. A. Maier, and J. K. Yang, *Nano Lett.* **11**, 1323 (2011).

[12] H. Duan, A. I. Fernández-Domínguez, M. Bosman, S. A. Maier, and J. K. Yang, *Nano Lett.* **12**, 1683 (2012).

[13] J. A. Scholl, A. García-Etxarri, A. L. Koh, and J. A. Dionne, *Nano Lett.* **13**, 564 (2013).

[14] S. Mukherjee, F. Libisch, N. Large, O. Neumann, L. V. Brown, J. Cheng, J. B. Lassiter, E. A. Carter, P. Nordlander, and N. J. Halas, *Nano Lett.* **13**, 240 (2013).

[15] S. Griffin, N. P. Montoni, G. Li, P. J. Straney, J. E. Millstone, D. J. Masiello, and J. P. Camden, *J. Phys. Chem. Lett.* **7**, 3825 (2016).

[16] G. Li, C. Cherqui, N. W. Bigelow, G. Duscher, P. J. Straney, J. E. Millstone, D. J. Masiello, and J. P. Camden, *Nano Lett.* **15**, 3465 (2015).

[17] J. A. Fan, C. Wu, K. Bao, J. Bao, R. Bardhan, N. J. Halas, V. N. Manoharan, P. Nordlander, G. Shvets, and F. Capasso, *Science* **328**, 1135 (2010).

[18] B. Ögüt, N. Talebi, R. Vogelgesang, W. Sigle, and P. A. van Aken, *Nano Lett.* **12**, 5239 (2012).

[19] C. Cherqui, N. W. Bigelow, A. Vaschillo, H. Goldwyn, and D. J. Masiello, *ACS Photonics* **1**, 1013 (2014).

[20] C. Cherqui, Y. Wu, G. Li, S. C. Quillin, J. A. Busche, N. Thakkar, C. A. West, N. P. Montoni, P. D. Rack, J. P. Camden, and D. J. Masiello, *Nano Lett.* **16**, 6668 (2016).

[21] N. P. Montoni, S. C. Quillin, C. Cherqui, and D. J. Masiello, *ACS Photonics* **5**, 3272 (2018).

[22] U. Fano, *Phys. Rev.* **124**, 1866 (1961).

[23] E. N. Lassettre, *Radiat. Res. Suppl.* **1**, 530 (1959).

[24] E. Lassettre, M. Krasnow, and S. Silverman, *J. Chem. Phys.* **40**, 1242 (1964).

[25] A. E. Miroshnichenko, S. Flach, and Y. S. Kivshar, *Rev. Mod. Phys.* **82**, 2257 (2010).

[26] Y.-C. Liu, B.-B. Li, and Y.-F. Xiao, *Nanophotonics* **6**, 789 (2017).

[27] N. Thakkar, M. T. Rea, K. C. Smith, K. D. Heylman, S. C. Quillin, K. A. Knapper, E. H. Horak, D. J. Masiello, and R. H. Goldsmith, *Nano Lett.* **17**, 6927 (2017).

[28] K. D. Heylman, N. Thakkar, E. H. Horak, S. C. Quillin, C. Cherqui, K. A. Knapper, D. J. Masiello, and R. H. Goldsmith, *Nat. Photonics* **10**, 788 (2016).

[29] M. V. Rybin, D. S. Filonov, P. A. Belov, Y. S. Kivshar, and M. F. Limonov, *Sci. Rep.* **5**, 8774 (2015).

[30] M. F. Limonov, M. V. Rybin, A. N. Poddubny, and Y. S. Kivshar, *Nat. Photonics* **11**, 543 (2017).

[31] H. Lu, X. Liu, D. Mao, and G. Wang, *Opt. Lett.* **37**, 3780 (2012).

[32] S. Simoncelli, Y. Li, E. Cortés, and S. A. Maier, *Nano Lett.* **18**, 3400 (2018).

[33] P. Alonso-Gonzalez, M. Schnell, P. Sarriugarte, H. Sobhani, C. Wu, N. Arju, A. Khanikaev, F. Golmar, P. Al bella, L. Arzubiaga, F. Casanova, L. E. Hueso, P. Nordlander, G. Shvets, and R. Hillenbrand, *Nano Lett.* **11**, 3922 (2011).

[34] M. Wang, A. Krasnok, T. Zhang, L. Scarabelli, H. Liu, Z. Wu, L. M. Liz-Marzán, M. Terrones, A. Alù, and Y. Zheng, *Adv. Mater.* **30**, 1705779 (2018).

[35] A. Lovera, B. Gallinet, P. Nordlander, and O. J. Martin, *ACS Nano* **7**, 4527 (2013).

[36] F. Shafiei, F. Monticone, K. Q. Le, X.-X. Liu, T. Hartsfield, A. Alù, and X. Li, *Nat. Nanotechnol.* **8**, 95 (2013).

[37] F. López-Tejeira, R. Paniagua-Domínguez, R. Rodríguez-Oliveros, and J. Sánchez-Gil, *New J. Phys.* **14**, 023035 (2012).

[38] N. Verellen, F. López-Tejeira, R. Paniagua-Domínguez, D. Vercruyse, D. Denkova, L. Lagae, P. Van Dorpe, V. V. Moshchalkov, and J. A. Sánchez-Gil, *Nano Lett.* **14**, 2322 (2014).

[39] F. Hao, Y. Sonnefraud, P. V. Dorpe, S. A. Maier, N. J. Halas, and P. Nordlander, *Nano Lett.* **8**, 3983 (2008).

[40] J. Göres, D. Goldhaber-Gordon, S. Heemeyer, M. A. Kastner, H. Shtrikman, D. Mahalu, and U. Meirav, *Phys. Rev. B* **62**, 2188 (2000).

[41] A. Bärnthaler, S. Rotter, F. Libisch, J. Burgdörfer, S. Gehler, U. Kuhl, and H.-J. Stöckmann, *Phys. Rev. Lett.* **105**, 056801 (2010).

[42] S. Rotter, F. Libisch, J. Burgdörfer, U. Kuhl, and H.-J. Stöckmann, *Phys. Rev. E* **69**, 046208 (2004).

[43] N. W. Bigelow, A. Vaschillo, J. P. Camden, and D. J. Masiello, *ACS Nano* **7**, 4511 (2013).

[44] S. M. Collins, O. Nicoletti, D. Rossouw, T. Ostasevicius, and P. A. Midgley, *Phys. Rev. B* **90**, 155419 (2014).

[45] A. Losquin and M. Kociak, *ACS Photonics* **2**, 1619 (2015).

[46] D. Rossouw, M. Couillard, J. Vickery, E. Kumacheva, and G. Botton, *Nano Lett.* **11**, 1499 (2011).

[47] O. Nicoletti, M. Wubs, N. A. Mortensen, W. Sigle, P. A. Van Aken, and P. A. Midgley, *Opt. Express* **19**, 15371 (2011).

[48] D. Rossouw and G. A. Botton, *Phys. Rev. Lett.* **110**, 066801 (2013).

[49] M. N'Gom, J. Ringnalda, J. F. Mansfield, A. Agarwal, N. Kotov, N. J. Zaluzec, and T. B. Norris, *Nano Lett.* **8**, 3200 (2008).

[50] J. Martin, M. Kociak, Z. Mahfoud, J. Proust, D. Gérard, and J. Plain, *Nano Lett.* **14**, 5517 (2014).

[51] Y. Wu, Z. Hu, X.-T. Kong, J. C. Idrobo, A. G. Nixon, P. D. Rack, D. J. Masiello, and J. P. Camden (to be published).

[52] See Supplemental Material at <http://link.aps.org/supplemental/10.1103/PhysRevLett.123.177401> for information on sample preparation, EELS measurements, data preparation, additional measurements, theoretical details of the model, and justification for product ansatz in Eq. (6).

[53] J. D. Jackson, *Classical Electrodynamics*, 3rd ed. (John Wiley & Sons, New York, 1999).

[54] R. H. Ritchie, *Phys. Rev. B* **106**, 874 (1957).

[55] C. Sönnichsen, Ph. D. thesis, Ludwig Maximilians Universität, 2001.

[56] S. R.-K. Rodriguez, *Eur. J. Phys.* **37**, 025802 (2016).

[57] L. Novotny, *Am. J. Phys.* **78**, 1199 (2010).